Precision Engineering 48 (2017) 83–97

Contents lists available at ScienceDirect

Precision Engineering

journal homepage: www.elsevier.com/locate/precision

Modeling and optimal design of circular-arch flexible structure with radial-freedom considering geometry and material selection simultaneously

Yuyan CAO*, Zhichen WANG, Chao ZHOU

Department of opto-electrical detection, Changchun Institute of Optics, Fine Mechanics and Physics, Chinese Academy of Sciences, Jilin Province 130033, China

ARTICLE INFO

Article history:
Received 13 June 2016
Received in revised form
13 November 2016
Accepted 15 November 2016
Available online 9 December 2016

Keywords:
Circular-arch
Generalized formulation
Variational principle
Optimization

ABSTRACT

The circular-arch flexible structure is widely used in various fields, especially the support structure of the optical mirrors. This paper aims to present a generalized formulation of the circular-arch flexible structure and a continuous method to optimize this flexible structure considering the material selection and geometry simultaneously. First, an analytical model based on the variational principle is derived for calculating the radial and tangential stiffness of the flexible element, and then the generalized formulation of the integral flexible structure is obtained by considering force equilibrium and compatible deformation. Second, the structural optimization is implemented by combining the material selection and geometrical parameters, where the continuous artificial variables are used to represent the selected material. Finally, the experimental and numerical examples are given to verify the analytical formulation and the optimization scheme. The experimental and FE simulation results of the flexible element and the integral flexible structure indicate that the presented mechanical model is capable of capturing the linear behavior. For the geometrical nonlinear deformation, there exist some errors. And the optimization results demonstrate that the presented scheme is able to obtain the discrete material design and the optimal geometry.

1. Introduction

The circular-arch flexible structure presented in this paper is composed by several identical shallow arches that act as the flexible elements. It can be seen as a special type of flexure hinge with radial freedom. Flexible structures have been widely used in a large number of fields with high precision requirements, such as optical structure [1], gyroscopes [2], actuators and sensors [3], micro/nano precision positioning stages [4,5], grippers and manipulators [6]. The wide-spread use of these precision flexible structures is due to the advantages they offer: (i)achieving high precision and repeatability since there is no friction, (ii)being easy to fabricate and maintain, which results in its low production cost [7].

Despite these advantages mentioned above, the mechanical model of the flexible structure is very complicated especially when many of them work together [8]. Many mathematical models have been developed to describe the mechanical behavior of the flexible structure. Paros and Weisbord [2] introduced an analytical model for calculating the compliances of single-axis and two-axis circular flexure hinges with constant cross-section in terms of deflections and rotations produced through bending and axial loading in their fundamental work. According to the theory of Paros and Weisbord [2], Smith et al. [9] introduced the approximate compliance equations for symmetric elliptic flexure hinge. Wu and Zhou [10] adopted the integration of linear differential equations of a beam to derive the concise compliance equation for flexure hinge. Lobontiu et al. [11] developed closed-form compliance equations for symmetric corner-filleted flexure hinges by using Castigliano's second theorem and made a comparison with the right circular flexure hinges, the results of which were confirmed by the finite element simulation and experiments. Lobontiu and Garcia [12] proposed a new type of two-axis flexible structure and developed a generic formulation in terms of the geometric curves defining the two notches. Lobontiu and Garcia [13] have formulated a closed-form equation for displacement and stiffness calculation of the planar compliant mechanisms using the strain energy and Castigliano's displacement theorem, and studied the performance of amplifying compliant mechanisms based on Lagrange's multipliers and Kuhn-Tucker conditions. Hopkins and Culpepper [14] [15] proposed freedom

* Corresponding author.

http://dx.doi.org/10.1016/j.precisioneng.2016.11.008
0141-6359/

and constraint topologies(FACT) synthesis method for compliant mechanism design, which utilizes a comprehensive library of geometric shapes that allow designers to visualize the quantitative relationships between all possible compliant mechanism design concepts and all possible motions for any given design problem. Hao [16] designed a class of single-axis translational flexure guiding mechanism. The wire beams were used as the distributed compliance module, which could avoid constraint stiffness decrease over the primary motion. However, most of them mentioned above mainly focus on the flexible structures with various shapes, and the researchers prefer to use the finite element method to verify the analytical model due to the limited experimental data available [12,17,18]. The circular-arch flexible structure, which is widely used in optical equipments, has received less attention. The concept of circular-arch flexible structure was first introduced by Yolder [19] and was adopted and improved by several researchers [20–22]. Yolder takes advantage of the radial freedom of such flexible structure to design the lens mounting structures. This flexible structure can be seen as the combination of discrete flexible elements, either the straight beam or the curved one. However, few researches focus on its analytical theory. Lim et al. [23], using Euler-Bernoulli theory and Timoshenko theory, derived the bending solution of a curved beam which can be seen as an element of this circular-arch flexible structure. Ahuett-Garza et al. [24] explored the use of curved beams as large displacement hinges in planar compliant mechanisms to overcome the limited deformation range of conventional hinge, and introduced the analytical expressions that predict deflections under different types of loads.

Designing this circular-arch flexible structure includes selecting the best materials and determining the optimal geometrical parameters. In order to obtain the optimal combination of geometry and material, the geometry optimization and material selection should be considered simultaneously. As mentioned in the literatures [25] [26], the material selection problem refers to the discrete optimization problem that is not amenable to the gradient-based algorithms, thus its solving efficiency is low. To avoid this, the discrete material selection should be relaxed to the continuous optimization problem. Hvejsel and Lund [25] and Hvejsel et al. [26] presented two multi-material interpolation schemes to relax the original discrete material selection problem, and then realized the simultaneous topology and material design. Kennedy and Martins [27] presented a relaxation technique for the layered composite structures with discrete layer ply-angles. The linear and nonlinear constraints are introduced to force the continuous artificial variables to attain the values 0/1. Kennedy [28] proposed an efficient gradient-based algorithm for the discrete thickness optimization problems. The piecewise constraint penal functions are imposed on the intermediate designs. Stegmann and Lund [29] proposed the discrete material optimization methods for multi-material distribution and lamination sequence design problems.

This paper is organized as follows. In Section 2, the mechanical model of the flexible element is derived using the variational principle. Based on the element model, the generalized formulation of the integral flexible structure is obtained. The implementation of the flexible structure optimization considering the material selection and geometry simultaneously is presented in Section 3. The experimental and numerical verification examples are described in Section 4. Finally, the conclusions are discussed in Section 5.

2. Mechanical formulation

It is known that the mirror's surface precision exerts great effect on the performance of the optical system and is determined by many factors, where the support structure is a key one [30]. The mirror, especially for the large one, needs a complicated support structure to hold it in the required surface precision and in the proper position regardless of the thermal or mechanical stress of the structure [31]. This indicates that the presence of mechanical constraints limits the motion of the mirror. The ideal mechanical constraints, including the lateral and axial constraints, should be kinematic, as Fig. 1 shows. That is to say all six degrees of freedom(DOFs) (three translations and three rotations, *dx*, *dy*, *dz*, *Rotx*, *Roty*, *Rotz*) would be independently constrained without any redundancy [19]. In order to fully constrain the mirror's motion, the support structure should introduce six constraints. From Fig. 1, it can be found that the axial support constrains three DOFs, *dz*, *Rotx*, *Roty*, and the lateral support constrains two DOFs, *dx*, *dy*. The last DOFs, *Rotz*, is constrained by the rotational constraint, which is not shown in Fig. 1. Since it contacts with the other structural component through the spherical surface(see Fig. 1b), the lateral support would not introduce other constraints except *dx* and *dy*. Usually, the mirror and its support structure have different thermal expansion coefficients(CTEs), so the thermal stress between their contact surface will be inevitable. Since the stiffness of the circular-arch

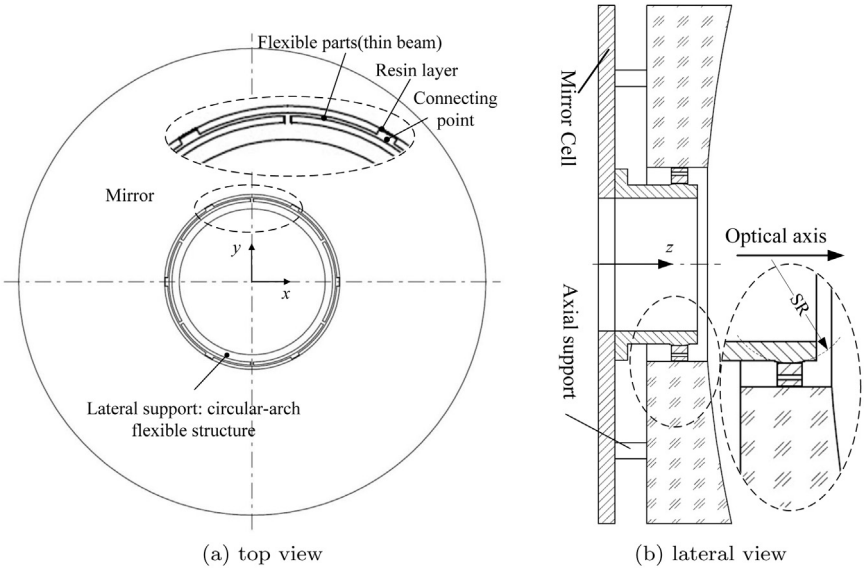

Fig. 1. The mirror and its supports

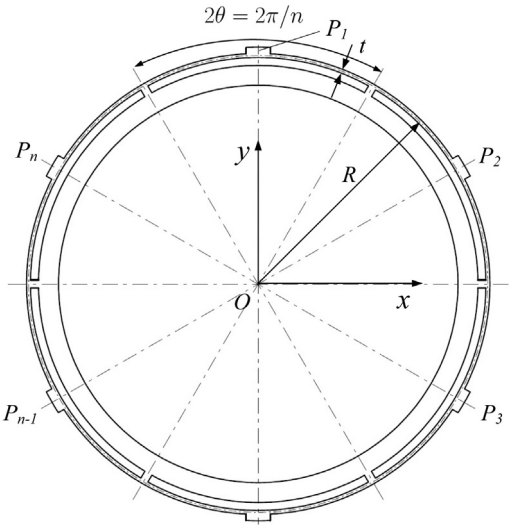

Fig. 2. The circular-arch flexible structure

flexible structure, which will be discussed in the following section, is high enough when it acts as a whole part, and a certain compliance exists in each flexible element, it may be the best candidate to offset the thermal stress caused by temperature variation. When the drastic temperature variation occurs, the deformation will mainly take place in the slender parts of this flexible structure. The thermal stress mainly focuses on the vicinity of the connecting points, so it will not result in large structure deformation or stress. The circular-arch flexible structure of a particular case with six arches is shown in Fig. 2. It can be tailored to various configurations, such as different shapes of connecting point and number of arches, to meet specific design requirements, as is shown in Fig. 3. The integral stiffness of this flexible structure is affected by several factors including the number of the arches or connecting points, the geometry and material parameters, mounting angle, etc(see Fig. 2). The stiffness and compliance of this flexible structure are vital to the structure design and system performance. Therefore, this section discusses the closed-form stiffness formulation for this flexible structure. With the in-plane stiffness playing a major role in the lateral support of the mirror, our main efforts focus on the in-plane property rather than the out-of-plane stiffness. Firstly, the variational principle is used to derive the stiffness of the flexible element. Secondly, the generalized formulation of the integral flexible structure is obtained based on the element model. The details are described as follows.

2.1. The analytical model of the flexible element

From Fig. 2, it is easily found that this circular-arch flexible structure consists of several identical flexible parts symmetrical in the rotational direction, and each part can be seen as an individual flexible element, a curved beam, as is shown in Fig. 4. The interaction load between the flexible element and the mirror is transfered through the connecting point. Compared with that of the circular-arch flexible structure, the elastic deformation of the mirror is tiny enough, so the mirror can be seen as a rigid body when we derive the stiffness of this flexible structure. Since the connecting point of the flexible structure is mechanically connected(through the epoxy resin bonding) to the mirror which experiences tiny deformation, there is no relative rotation DOF at the bonding position between the mirror and the connecting point of the flexible structure. Based on the above conditions, the rotational constraint $Rot_z = 0$ should be added, at the bonding position, to the model of the flexible structure when it is considered individually. In addition, the connecting point can be assumed as a rigid body when its size, $l_a \times l_b$, is reasonable, therefore the external loads applied to the connecting point, which can be decomposed as F_r and F_t, are equivalent to those applied to point C(see Fig. 4). That means the original model Fig. 4(a) can be simplified to the model shown in Fig. 4(b). The reasonable size of the connecting point and the validity of the assumption are verified in

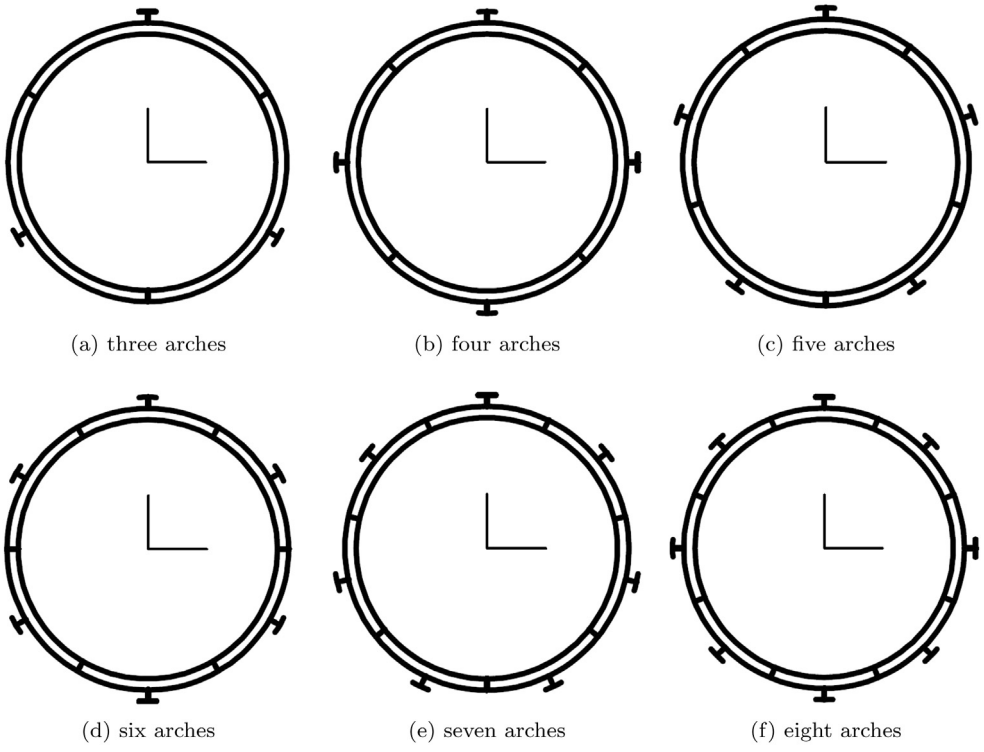

Fig. 3. The flexible structures with different number of arches

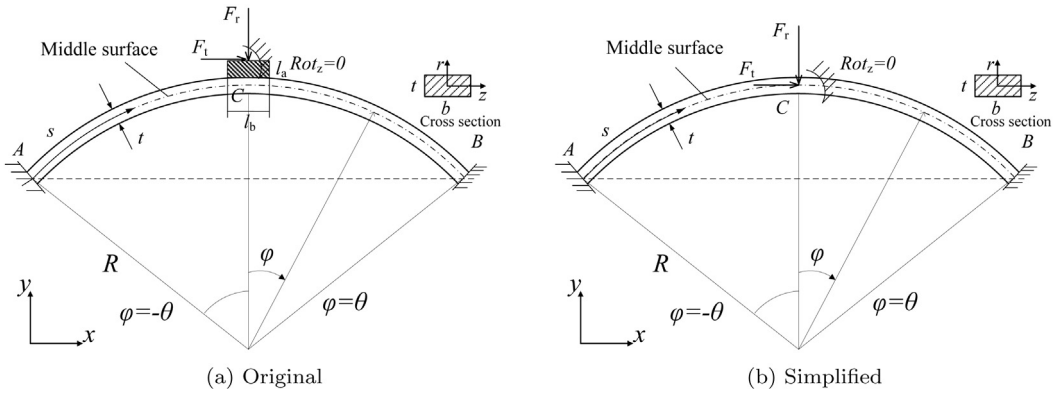

Fig. 4. The flexible element

Section 4. From Fig. 4, the individual flexible element exhibits constant curvature, adding significant complexity to the beam problem by raising the order of the governing equation of the slender beam from four to six. This flexible element is defined by the radius of curvature of the middle surface R, the central angle θ, the thickness t, and the constant out-of-plane width b, where the central angle θ is determined by the arch number of this flexible structure, n.

Here, the flexible element(curved beam) is characterized by its middle surface, which is defined by the polar coordinate s

$$s = R\varphi(-\theta \le \varphi \le \theta) \tag{1}$$

The in-plane normal strain is [32]

$$\epsilon = \frac{1}{1+r/R}(\epsilon_0 + r\kappa_0) \approx \epsilon_0 + r\kappa_0 \tag{2}$$

where r is the thickness coordinate measured from middle surface. Note that Euler's beam theory is used here, and the Lamé parameter $1/(1+r/R)$ is neglected.

The middle surface normal strain ϵ_0 and curvature changes κ_0 are [23] [32]

$$\epsilon_0 = \frac{du}{ds} + \frac{w}{R} = \frac{1}{R}(\frac{du}{d\varphi} + w) \tag{3}$$

$$\kappa_0 = -\frac{d^2w}{ds^2} + \frac{1}{R}\frac{du}{ds} = \frac{1}{R^2}(-\frac{d^2w}{d\varphi^2} + \frac{du}{d\varphi}) \tag{4}$$

where u and w are the displacements of the middle surface in radial and tangential directions respectively.

Based on the virtual work principle, the in-plane governing equation for the flexible element(Shown in Fig. 4) during the elastic deformation can be derived. That is

$$\delta\Pi = \delta U + \delta V = \int_{-\theta}^{\theta}\int_{A}\sigma\delta\epsilon R dA d\varphi - \delta[F_r w_0 + F_t u_0] = \int_{-\theta}^{\theta}[\frac{EA}{R}(\frac{du}{d\varphi}+w)(\frac{d\delta u}{d\varphi}+\delta w) + \frac{EI}{R^3}(\frac{du}{d\varphi} - \frac{d^2w}{d\varphi^2})(\frac{d\delta u}{d\varphi} - \frac{d^2\delta w}{d\varphi^2})]d\varphi - F_r\delta w_0 - F_t\delta u_0 = 0 \tag{5}$$

where Π is the total potential energy, U is the strain energy, V is the external work done by the concentrated loads F_r and F_t, u_0 and w_0 are the tangential and radial displacements at the loading point.

The integral will be evaluated part by part with the help of partial integration with respect to φ, and the δU can be rewritten as

$$\begin{aligned}
\delta U = &\int_{-\theta}^{0}([\frac{EA}{R}(\frac{du}{d\varphi}+w) - \frac{EI}{R^3}(\frac{d^3u}{d\varphi^3} - \frac{d^4w}{d\varphi^4})]\delta w - [\frac{EA}{R}(\frac{d^2u}{d\varphi^2}+\frac{dw}{d\varphi}) + \frac{EI}{R^3}(\frac{d^2u}{d\varphi^2} - \frac{d^3w}{d\varphi^3})]\delta u)d\varphi \\
&+\int_{0}^{\theta}([\frac{EA}{R}(\frac{du}{d\varphi}+w) - \frac{EI}{R^3}(\frac{d^3u}{d\varphi^3} - \frac{d^4w}{d\varphi^4})]\delta w - [\frac{EA}{R}(\frac{d^2u}{d\varphi^2}+\frac{dw}{d\varphi}) + \frac{EI}{R^3}(\frac{d^2u}{d\varphi^2} - \frac{d^3w}{d\varphi^3})]\delta u)d\varphi \\
&+[\frac{EA}{R}(\frac{du}{d\varphi}+w) + \frac{EI}{R^3}(\frac{du}{d\varphi} - \frac{d^2w}{d\varphi^2})]\delta u|_{-\theta}^{0} + [\frac{EA}{R}(\frac{du}{d\varphi}+w) + \frac{EI}{R^3}(\frac{du}{d\varphi} - \frac{d^2w}{d\varphi^2})]\delta u|_{0}^{\theta} \\
&+\frac{EI}{R^3}(\frac{d^2u}{d\varphi^2} - \frac{d^3w}{d\varphi^3})\delta w|_{-\theta}^{0} + \frac{EI}{R^3}(\frac{d^2u}{d\varphi^2} - \frac{d^3w}{d\varphi^3})\delta w|_{0}^{\theta} - \frac{EI}{R^3}(\frac{du}{d\varphi} - \frac{d^2w}{d\varphi^2})\frac{d\delta w}{d\varphi}|_{-\theta}^{0} - \frac{EI}{R^3}(\frac{du}{d\varphi} - \frac{d^2w}{d\varphi^2})\frac{d\delta w}{d\varphi}|_{0}^{\theta}
\end{aligned} \tag{6}$$

Substituting Eq. (6) into Eq. (5), and considering the property that δu and δw are arbitrary in the interval $(-\theta, \theta)$, we have

$$\frac{EA}{R}(\frac{du}{d\varphi}+w) - \frac{EI}{R^3}(\frac{d^3u}{d\varphi^3} - \frac{d^4w}{d\varphi^4}) = 0 \tag{7}$$

$$\frac{EA}{R}(\frac{d^2u}{d\varphi^2}+\frac{dw}{d\varphi}) + \frac{EI}{R^3}(\frac{d^2u}{d\varphi^2} - \frac{d^3w}{d\varphi^3}) = 0 \tag{8}$$

Integrating the Eqs. (7) and (8), the displacements u and w can be obtained, as

$$w(\varphi) = \begin{cases} C_{41}\sin\varphi + C_{51}\cos\varphi - \dfrac{R^3}{EI}C_{31} \\ +\dfrac{1}{2}(\dfrac{R}{EA} + \dfrac{R^3}{EI})\varphi(C_{21}\sin\varphi - C_{11}\cos\varphi), \quad -\theta \le \varphi < 0 \\ C_{42}\sin\varphi + C_{52}\cos\varphi - \dfrac{R^3}{EI}C_{32} \\ +\dfrac{1}{2}(\dfrac{R}{EA} + \dfrac{R^3}{EI})\varphi(C_{22}\sin\varphi - C_{12}\cos\varphi), \quad 0 \le \varphi \le \theta \end{cases} \tag{9}$$

$$u(\varphi) = \begin{cases} C_{41}\cos\varphi - C_{51}\sin\varphi + \dfrac{R^3}{EI}C_{31}\varphi + \dfrac{1}{2}(\dfrac{R}{EA} + \dfrac{R^3}{EI})\varphi(C_{21}\cos\varphi + C_{11}\sin\varphi) \\ \dfrac{1}{2}(\dfrac{R}{EA} - \dfrac{R^3}{EI})(C_{21}\sin\varphi - C_{11}\cos\varphi) + C_{61}, \quad -\theta \le \varphi < 0 \\ C_{42}\cos\varphi - C_{52}\sin\varphi + \dfrac{R^3}{EI}C_{32}\varphi + \dfrac{1}{2}(\dfrac{R}{EA} + \dfrac{R^3}{EI})\varphi(C_{22}\cos\varphi + C_{12}\sin\varphi) \\ \dfrac{1}{2}(\dfrac{R}{EA} - \dfrac{R^3}{EI})(C_{22}\sin\varphi - C_{12}\cos\varphi) + C_{62}, \quad 0 \le \varphi \le \theta \end{cases} \tag{10}$$

where C_{ij} are constants that relate to the loads F_r and F_t.

The unknown constants C_{ij} can be obtained by introducing the boundary conditions. Considering Eqs. (5) and (6) and the continuous conditions concerning u and w, we have the following boundary conditions

$$\begin{cases} u = 0, w = 0, \dfrac{dw}{d\varphi} = 0, \quad \text{at} \quad \varphi = -\theta \quad \text{and} \quad \varphi = \theta & \text{(11a)} \\ u(0_-) = u(0_+), w(0_-) = w(0_+), \dfrac{dw(0_-)}{d\varphi} = \dfrac{dw(0_+)}{d\varphi} = 0 & \text{(11b)} \\ \dfrac{EI}{R^3}[(\dfrac{du^2(0_-)}{d\varphi^2} - \dfrac{dw^3(0_-)}{d\varphi^3}) - (\dfrac{du^2(0_+)}{d\varphi^2} - \dfrac{dw^3(0_+)}{d\varphi^3})] - F_r = 0 & \text{(11c)} \\ \dfrac{EA}{R}[(\dfrac{du(0_-)}{d\varphi} + w(0_-)) - (\dfrac{du(0_+)}{d\varphi} + w(0_+))] + \dfrac{EI}{R^3}[(\dfrac{du(0_-)}{d\varphi^2} - \dfrac{d^2w(0_-)}{d\varphi^2}) & \\ \qquad -(\dfrac{du(0_+)}{d\varphi} - \dfrac{d^2w(0_+)}{d\varphi^2})] - F_t = 0 & \text{(11d)} \end{cases}$$

where the first two conditions are obtained directly, and the other two conditions are obtained from the variation equation (5). Substituting the above 12 conditions into Eqs. (9)(10), the unknown constants C_{ij} can be derived.

Since the external loads are applied to the central point C(see Fig. 4), the deformation of the loading point C may be of great interest. Let $\varphi = 0$, and the deformation of point C $w(0)$, $u(0)$ can be obtained from Eqs. (9)(10), as

$$w(0) = \frac{F_r R(R^2+\rho)}{2EI} \frac{(R^2+\rho)\theta(\theta^2+\cos^2\theta-1) + 4R^2(\sin\theta-\theta)(1-\cos\theta)}{(R^2+\rho)(2\theta^2+\theta\sin 2\theta) - 4R^2\sin^2\theta} \tag{12}$$

$$u(0) = \frac{F_t R^3}{2EI} \frac{(R^2+\rho)\theta(\theta^2+\cos^2\theta-1) + 4R^2(\sin\theta-\theta)(1-\cos\theta)}{(R^2+\rho)(\theta^2+\cos^2\theta-1)} \tag{13}$$

where $\rho = I/A$.

The Eqs. (12)(13) show that at point C the radial load F_r only causes radial deformation and the tangential load F_t only causes tangential deformation. Let K_r and K_t denote the stiffnesses of this flexible element in radial and tangential directions respectively, which can be obtained from Eqs. (12)(13), as

$$K_r = \frac{F_r}{w(0)} = E\overline{K}_r(R, \theta, b, t) \tag{14}$$

$$K_t = \frac{F_t}{u(0)} = E\overline{K}_t(R, \theta, b, t) \tag{15}$$

where, $\overline{K}_r$, $\overline{K}_t$ are the stiffness coefficients unrelated to the material.

From Eqs. (14) and (15), the radial and tangential stiffness of the flexible element are directly related to the modulus E, width b, thickness t, radius R, and the arch number n.

2.2. The integral stiffness formulation of the circular-arch flexible structure

Since the DOFs, dx and dy, of the inner ring of this circular-arch flexible structure is constrained by the other structural component through spherical surface(shown in Fig. 1), the inner ring can be seen as fixed when we mainly consider the in-plane deformation. From Fig. 2, the total external load imposed on this flexible structure is assumed in the y direction. The force and displacement analysis of the circular-arch flexible structure are shown in Fig. 5, where β is the initial mounting angle.

In Fig. 5(a), $F_1, F_2, \cdots, F_n$ are used to denote the force imposed on the connecting points $P_1, P_2, \cdots, P_n$ respectively, F_{ir}, F_{it}, F_{ix} and F_{iy} are the force components of F_i in radial, tangential, x-axis and y-axis directions. The force component $F_{ix}, F_{iy}(i = 1, 2, \cdots, n)$ are expressed in terms of tangential and radial components as

$$F_{ix} = F_{it}\cos(\beta + (i-1)\frac{2\pi}{n}) - F_{ir}\sin(\beta + (i-1)\frac{2\pi}{n}) \tag{16}$$

$$F_{iy} = -F_{it}\sin(\beta + (i-1)\frac{2\pi}{n}) - F_{ir}\cos(\beta + (i-1)\frac{2\pi}{n}) \tag{17}$$

Then summing the force at all points, it follows

$$F_x = \sum_{i=1}^{n} F_{ix} = \sum_{i=1}^{n}(F_{it}\cos(\beta + (i-1)\frac{2\pi}{n}) - F_{ir}\sin(\beta + (i-1)\frac{2\pi}{n})) \tag{18}$$

$$F_y = \sum_{i=1}^{n} F_{iy} = -\sum_{i=1}^{n}(F_{it}\sin(\beta + (i-1)\frac{2\pi}{n}) + F_{ir}\cos(\beta + (i-1)\frac{2\pi}{n})) \tag{19}$$

Since we have assumed that the external load F is acted in the y-axis direction, then

$$F = F_y, F_x = 0 \tag{20}$$

Let δ_{ir} and δ_{it} denote the displacement components of points $P_i(i = 1, 2, \cdots, n)$ in radial and tangential directions(see Fig. 5(b)), then the displacement components δ_{iy} can be expressed as

$$\delta_{iy} = -\delta_{it}\sin(\beta + (i-1)\frac{2\pi}{n}) - \delta_{ir}\cos(\beta + (i-1)\frac{2\pi}{n}) \tag{21}$$

Since the arch of the flexible structure is equally spaced and $F_x = 0$, there will be no displacement in the x direction for each point $P_i(i = 1, 2, \cdots, n)$. It follows that

$$\delta_{ix} = -\delta_{it}\cos(\beta + (i-1)\frac{2\pi}{n}) + \delta_{ir}\sin(\beta + (i-1)\frac{2\pi}{n}) = 0 \tag{22}$$

When the elastic deformation of the mirror(Fig. 1) is compared with that of this flexible structure, it is tiny enough and the mirror can be seen as a rigid body. Then the connecting points $P_i(i = 1, 2, \cdots, n)$ must have the same displacements $\delta_y = \delta_{iy}$. From Eqs. (21)(22), we have

$$\delta_y = -\delta_{ir}\frac{1}{\cos(\beta + (i-1)\frac{2\pi}{n})} \tag{23}$$

According to Eqs. (14) and (15), we have

$$F_{ir} = K_r\delta_{ir}, F_{it} = K_t\delta_{it}, \tag{24}$$

From Eqs. (19)(23) and (24), we have

$$F = \delta_y(K_t\sum_{i=1}^{n}\sin^2(\beta + (i-1)\frac{2\pi}{n}) + K_r\sum_{i=1}^{n}\cos^2(\beta + (i-1)\frac{2\pi}{n})) \tag{25}$$

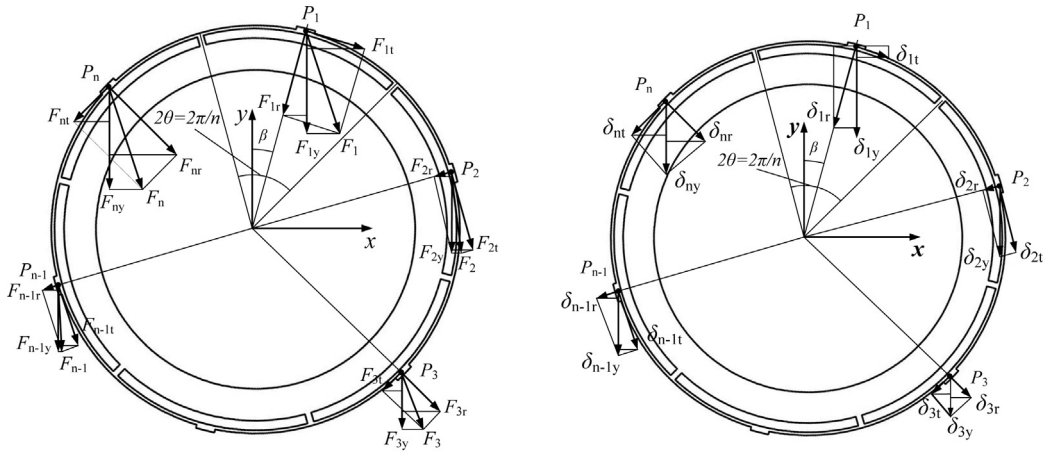

(a) The force decomposition (b) The displacement decomposition

Fig. 5. The force and displacement analysis of the circular-arch flexible structure

For $n>2$, $\sum \sin^2(\beta+(i-1)\frac{2\pi}{n})$ and $\sum \cos^2(\beta+(i-1)\frac{2\pi}{n})$ are independent from the angle β and equal to $n/2$, then the integral stiffness of the circular-arch flexible structure K can be expressed as

$$K=\frac{n}{2}(K_t+K_r) \tag{26}$$

The Eq. (26) shows that the integral stiffness K is uniform in the rotational directions, which is a particular useful characteristic.

3. The optimal design of the circular-arch flexible structure considering continuous and discrete variables simultaneously

The optimal design of this flexible structure entails choosing the best material and determining the optimal geometrical parameters and configuration. The previous studies mainly focus on assuming a material before optimizing the geometry or selecting the best material for an existing geometry of a structure. However, these approaches do not guarantee the optimal combination of geometry and material. The best choice should be considering geometry optimization and material selection simultaneously. Due to the physical property of the material, the allowable material parameters are restricted to a discrete set of values. The other parameters, such as the thickness t and out-of-plane width b, are continuous. Here, we should note that the central angle θ, determined by the arch number n, is also a discrete variable. Considering the complexity of the K_r and K_t, the various configurations of this flexible structure are treated separately. For each configuration, the optimal design is modeled as a linear or nonlinear mixed-integer programming problem. However, this optimization problem is not amenable to the gradient-based optimization method. Furthermore, the nonlinear mixed-integer programming problem is almost inevitably computationally expensive. Here, an efficient gradient-based technique is proposed to obtain the optimal solution for this mixed-integer problem. Based on the proposed method, the original mixed-integer problem can be relaxed into a continuous problem. This section focuses on the description of this gradient based technique.

3.1. The original mixed-integer optimization model

In the previous section, we have mentioned the mirror and its support structure(see Fig. 1), where the surface precision and optical axis position are important criteria to evaluate the performance of the mirror's support structure. The surface precision of the mirror is measured by Root Mean Square(RMS) error, which is defined as the mean deviation between the deformed shape and the desired shape. The RMS error is usually computed using the finite element simulation and it is unlikely to be expressed as an explicit function of the axial support, which is not considered in this work, or the lateral support. The optical axis position is measured by the rigid body displacement of the mirror. The mirror has two extreme working positions, the optical axis in horizontal and zenith directions (see Fig. 6). Within the range of these two positions, the mirror will undergo elastic deformation and rigid body displacement, resulting in the RMS error and optical axis deviation. The lateral support, a circular-arch flexible structure, is bonded to the central hole of the mirror using epoxy resin. Usually the thermal expansion coefficients of this flexible structure and mirror are different, and as a result, the thermal stress in their bonding area would cause extra elastic deformation when there is temperature difference. When the optical axis in horizontal direction, the mirror will suffer the maximum rigid body displacement caused by its gravity and by the flexibility of the circular-arch flexible structure. Obviously, these two cases mentioned above are contradictory. In terms of elastic deformation, the flexible structure should be designed as flexible as possible so as to minimize the stress between the flexible structure and the mirror caused by temperature variation. Accordingly, the mirror's RMS error is minimized. For the latter case, if the circular-arch flexible structure is flexible enough,

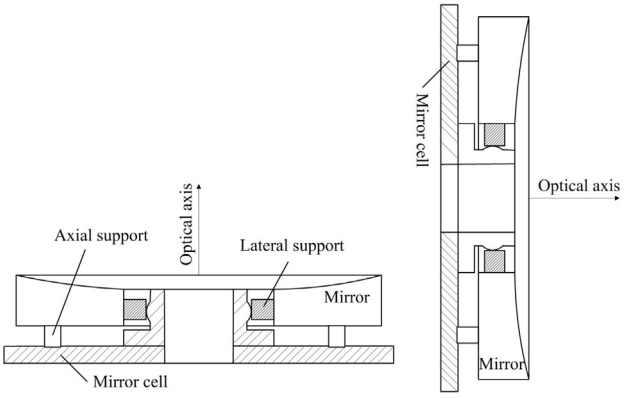

(a) The zenith position (b) The horizontal position

Fig. 6. The two extreme working positions

the rigid body displacement will be too large to meet the optical axis position requirements. Therefore, the flexible structure should be designed with less flexibility. In order to meet these two incompatible cases, this flexible structure should be properly designed using the optimization method.

Based on the above description, the best objective function should both include the thermal stress and the rigid body displacement at the same time. The following objective function is adopted to realize this purpose. That is

$$\Phi = \omega_1 \frac{H - h^L}{h^U - h^L} + \omega_2 \frac{G - g^L}{g^U - g^L} \tag{27}$$

where ω_1 and ω_2 are the weighted factors; $H = (\alpha - \alpha_m)^2 K_r$ denotes the thermal stress between the flexible structure and the mirror, α and α_m are the thermal expansion coefficients of the flexible structure and the mirror; $G = \frac{1}{n(K_r + K_t)/2}$ denotes the rigid body displacement; h^L and h^U are the minimum and maximum value of H, and g^L and g^U are the minimum and maximum value of G, which are used to normalize the objective function.

From Eqs. (14) and (15), the stiffness of the circular-arch flexible structure is affected by its elastic modulus E, geometrical parameters,R, t, b, and the arch number n. The material parameter E is limited to a set of discrete values, and a discrete variable ξ_i is introduced to represent the selection of a given candidate material

$$\xi_i = \begin{cases} 1 & \text{if material } i \text{ is selected} \\ 0 & \text{if not} \end{cases} \tag{28}$$

By using the discrete variable ξ_i, the structural design considering the material selection and geometry can be expressed as a nonlinear mixed-integer programming. That is

$$\begin{aligned} &set \quad n \\ &minimize \quad \Phi(\xi_i, b, t) = \omega \frac{H - h^L}{h^U - h^L} + (1 - \omega) \frac{G - g^L}{g^U - g^L} \\ &s.t. \begin{cases} \sum_{i=1}^{m} \xi_i = 1 \\ \xi_i \in \{0, 1\}, b \in [b_l, b_u], t \in [t_l, t_u] \end{cases} \end{aligned} \tag{29}$$

where $H = \sum_{i=1}^{m} \xi_i E_i (\alpha_i - \alpha_m)^2 \overline{K_r}$, $G = \frac{1}{n \sum_{i=1}^{m} E_i \xi_i (\overline{K_r} + \overline{K_t})/2}$; ξ_i is the binary variable that corresponds to the material; m is the number of candidate materials, E_i is the elastic modulus of ith candidate material; the equality constraints are used to avoid multiple materials being selected. If any variable attains 1, the remaining variables must be 0 in order for the equality to hold.

The problem Eq. (29) is a nonlinear mixed integer programming problem, where ξ_i is the discrete variables, and the others are continuous. The number of possible designs increases rapidly as the number of candidate materials increases. Evaluating all possible designs becomes inconvenient or intractable. By using the continuous variable $x_i \in [0, 1]$ to replace the discrete variable $\xi_i \in \{0, 1\}$, the mixed integer problem Eq. (29) can be relaxed to a continuous problem which can be solved using standard nonlinear programming algorithms. The interpolation schemes that have gained a large acceptance in the topology optimization community, are used here to relax the original problem. They are known as SIMP scheme (Solid Isotropic Material with Penalization) [33] and RAMP scheme (Rational Approximation of Material Properties) [34].

3.2. Material interpolation schemes

Since the material parameters are restricted to a discrete set of the candidate materials, considering the material parameter as a continuous design variable is meaningless as the optimal material may not exist. The material interpolation schemes should allow intermediate material variables during the optimizing process, but penalize intermediate variables so as to obtain distinct variables at the same time and eventually satisfying the original binary requirements. The material interpolation is regarded as a heuristic method that is viable as long as the final solution satisfies the binary condition, and the intermediate results are merely the artifact that we use to obtain the distinct results. The interpolation schemes popularly used in structural topology optimization are multiphase SIMP and Multiphase RAMP methods.

The SIMP scheme is a direct generalization scheme proposed for the interpolation between void and solid. Stegmann and Lund [29] has extended this scheme to multiple materials case. The expression of the SIMP interpolation scheme is

$$E = \sum_{i=1}^{m} x_i^p E_i, \quad p \geq 1 \tag{30}$$

where p is penal factor that controls the contribution of each material phase. For $p > 1$ the intermediate material selections are penalized.

The RAMP scheme was proposed as an alternative interpolation scheme for the two-phase topology optimization [34] The idea of this scheme is that a certain value of the penal factor yields a concave cost function which increases the probability of obtaining a distinct solution. The interpolation scheme is given by

$$E = \sum_{i=1}^{m} \frac{x_i}{1 + q(1 - x_i)} E_i, \quad q \geq 0 \tag{31}$$

where the penal parameter q is similar to that of p in the SIMP scheme.

Note that for $m = 2$, the generalized scheme (30)(31) reduce to the well known two-phase SIMP/RAMP scheme. For this particular case, the penal effects for different penal factors is shown in Fig. 7. From Fig. 7, the penal effect become obvious as the penal factors p, q increase.

3.3. The relaxed continuous optimization model

With the design variables $x_i (i = 1, 2, \cdots, m)$ and the SIMP or RAMP interpolation schemes, the optimization model (29) can be relaxed to the continuous nonlinear models, and the functions H and G are changed to

$$H = \sum_{i=1}^{m} x_i^p E_i (\alpha_i - \alpha_m)^2 \overline{K_r} \tag{32}$$

$$G = \frac{1}{n \sum_{i=1}^{m} E_i x_i^p (\overline{K_r} + \overline{K_t})/2} \tag{33}$$

where the model (32)(33) refers to SIMP scheme, and the RAMP based model is omited here.

Similar to the mixed-integer optimization model, the constraint $\sum x_i = 1$ is imposed on the continuous variables x_i. The constraint $\sum \xi_i = 1$ is sufficient to guarantee that only a single material is selected in the discrete case. However, in the continuous case, that constraint can not realize the same goal as in the discrete case, since it forces the design variables to remain only on a plane intersecting the coordinate axes at unity [27].

In the continuous case, to force the design toward a discrete solution, an extra non-linear constraint is introduced, as

$$\sum_{i=1}^{m} x_i^2 = 1 \tag{34}$$

The constraint Eq. (34) restricts the design variables x_i to a unit sphere. Satisfying the constraint Eq. (34), $\sum x_i = 1$, and $x_i \in [0, 1]$

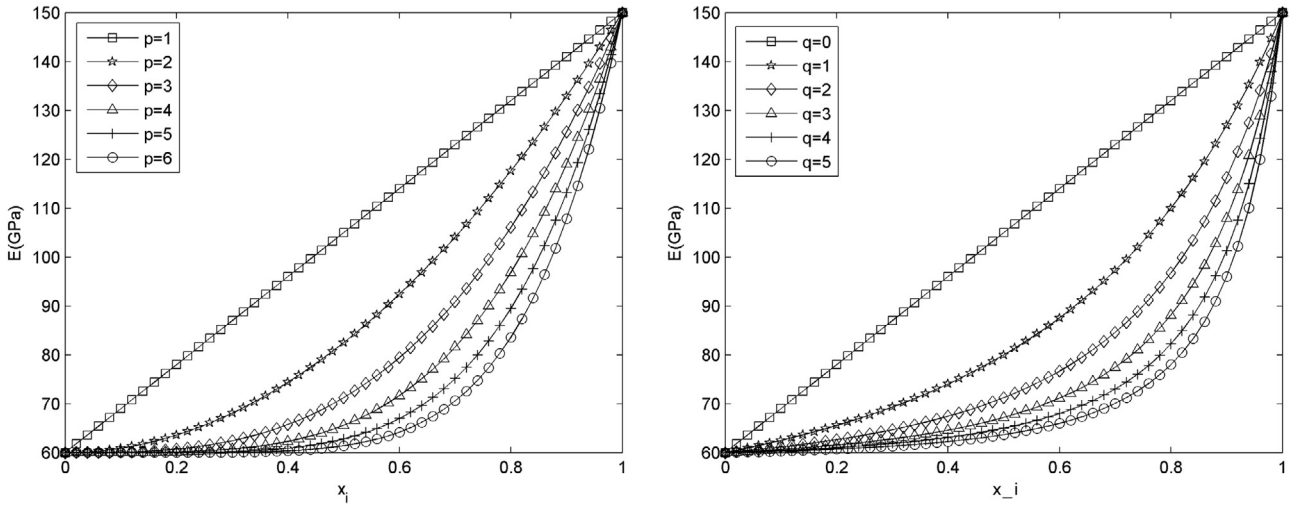

(a) SIMP scheme (b) RAMP scheme

Fig. 7. The material parameter E vs variable x_i for the SIMP/RAMP scheme

ensure that only one material is active. For a particular case, $m = 3$, the relation between linear and non-linear constraints is shown in Fig. 8, the upper limit on the design variables x_i can be dropped here.

Incorporating the non-linear constraint(34), the optimization model Eq. (29) can be rewritten as

$$\begin{aligned} &set \quad n \\ &minimize \quad \Phi(x_i, b, t) = \omega \frac{H - h^L}{h^U - h^L} + (1 - \omega)\frac{G - g^L}{g^U - g^L} \\ &s.t. \begin{cases} \sum_{i=1}^{m} x_i^2 = 1 \\ \sum_{i=1}^{m} x_i = 1 \\ b \in [b_l, b_u], t \in [t_l, t_u] \\ x_i \geq 0 \end{cases} \end{aligned} \tag{35}$$

where the equality constraint $\sum x_i = 1$ ensures that the design variables x_i fulfill the upper bound constraints, thus there is no need for an upper bound on the variables x_i. Since the model (35) is the continuous relaxation of (29), it is less constrained than (29). The feasible set of (29) is a subset of the feasible set of (35) [26].

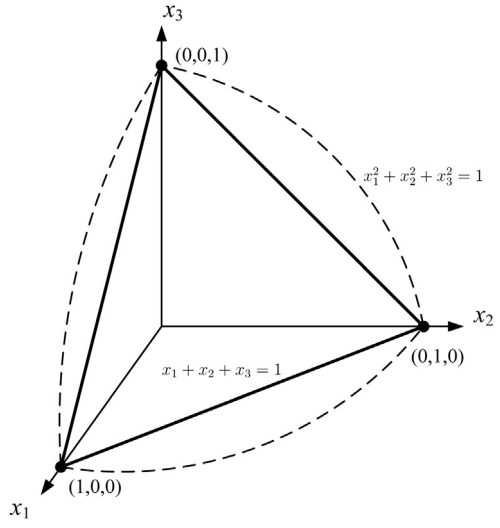

Fig. 8. The linear and non-linear constraint

To improve the computational efficiency, the non-linear constraint is expressed as a penalty function with penal factor γ. The modified objective function can be written as

$$\Phi(x_i, b, t) + \gamma(1 - \sum_{i=1}^{m} x_i^2) \tag{36}$$

Since $(\sum x_i)^2 \geq \sum x_i^2$, if the equality constraint $\sum x_i = 1$ is satisfied exactly, the penalty function in Eq. (36) is always positive, i.e. $1 - \sum x_i^2 \geq 0$.

Here, the SQP(Sequential Quadratic Programming) methods [35] is used to solve the optimization model (35). The flowchart for the optimization is shown in Fig. 9. Each optimization iteration starts from the previous solution. The small penal factor γ allows greater freedom to explore the design space. When γ increases, the design variables become difficult to change and finally converge to a discrete solution. The optimization process is terminated once the artificial design variables satisfy the discrete criterion. The optimization begins with the initial penal factor $\gamma_0 = 0$ and the initial design variables $x_i = 1/m (i = 1, 2, \cdots, m)$, which satisfies the equality constraint $\sum x_i = 1$ exactly.

4. Verification

This section aims to verify the theoretical formulation of the circular-arch flexible structure through experiments and finite element simulation concerning the flexible element and the integral flexible structure and to confirm the continuous optimization scheme through numerical simulation.

4.1. Model verification

At the beginning of Section 2, we have mentioned the model simplification, the foundation of the subsequent sections. It is necessary to first verify the effectiveness of this simplification shown in Fig. 4. Due to the symmetrical property of the flexible element, this simplification will not result in the radial stiffness error. The tangential stiffness error is mainly caused by the rigid body assumption of the connecting point and the shift of the loading point, which is determined by the size of the connecting point, $l_a \times l_b$.

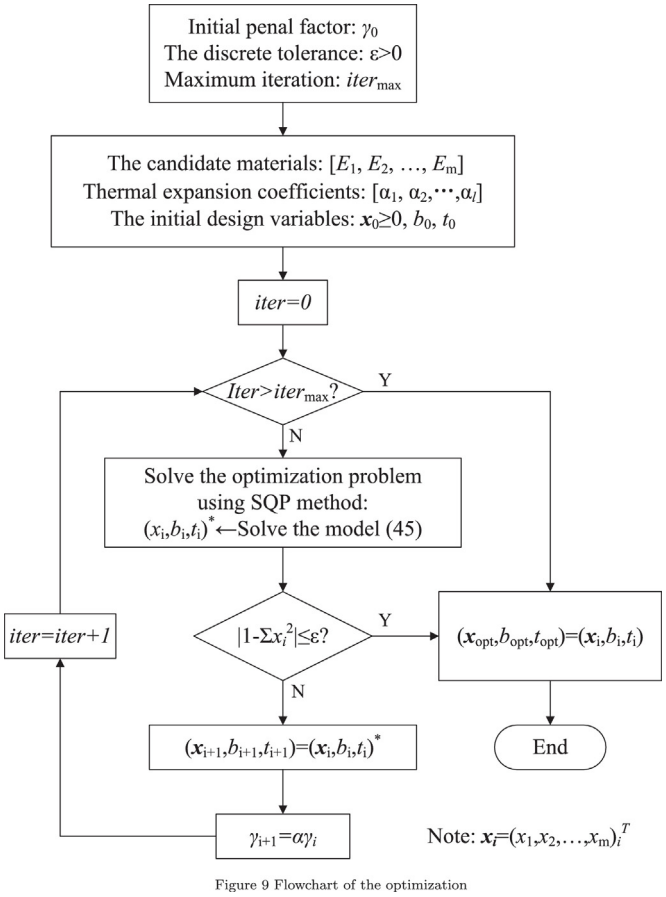

Fig. 9. Flowchart of the optimization

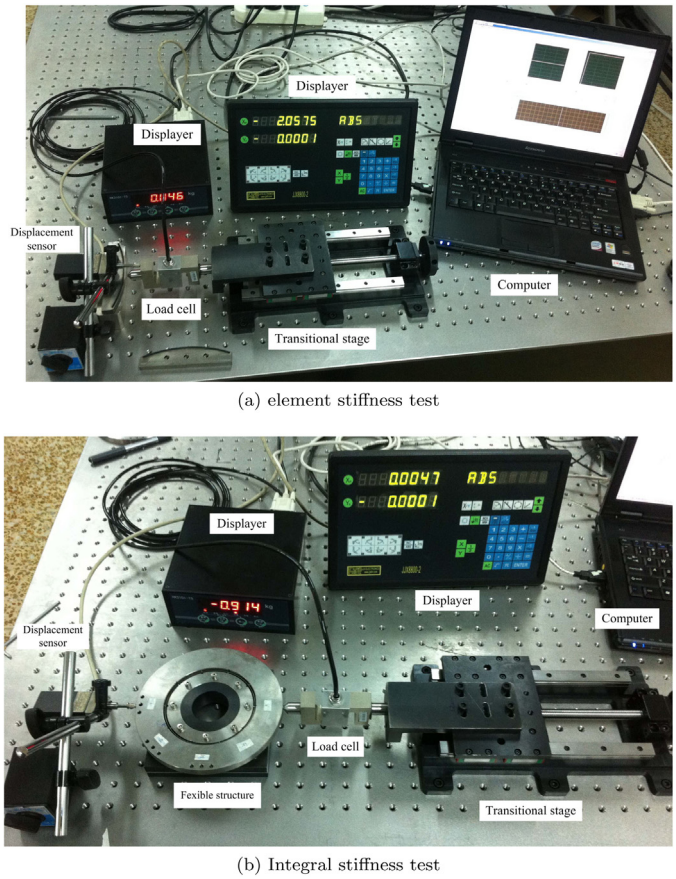

Fig. 11. The experimental set-up for stiffness test

Inappropriate design of the connecting point would lead to its noticeable deformation, which can not be neglected in the analytical model of the flexible element. For this point, the nonlinear FE simulations regarding the tangential stiffness of the flexible element with various l_a and l_b combinations are implemented. The FE models corresponding to the flexible element model Fig. 4(a) and its simplified model Fig. 4(b) are established respectively, where the geometrical and material parameters are the same with the specimen 1 # introduced in the following section. Then the tangential stiffness corresponding to the different l_a and l_b combinations are computed and compared with that of the simplified model. The tangential stiffness and the errors are shown in Fig. 10.

From Fig. 10, we can see that when $l_a < 3$ and $l_b > 2$, the tangential stiffness errors between the original model and its simplified model are less than 1% and varies insignificantly as l_a or l_b changes, which indicates that the simplified model Fig. 4(b) can be used to represent the original model Fig. 4(a). As we know, this type of structure is usually fabricated using high precision Electrical Discharge Machining(EDM) lathe. Its machining accuracy can reach to $5\mu m$, so the size requirements of the flexible element can be easily satisfied.

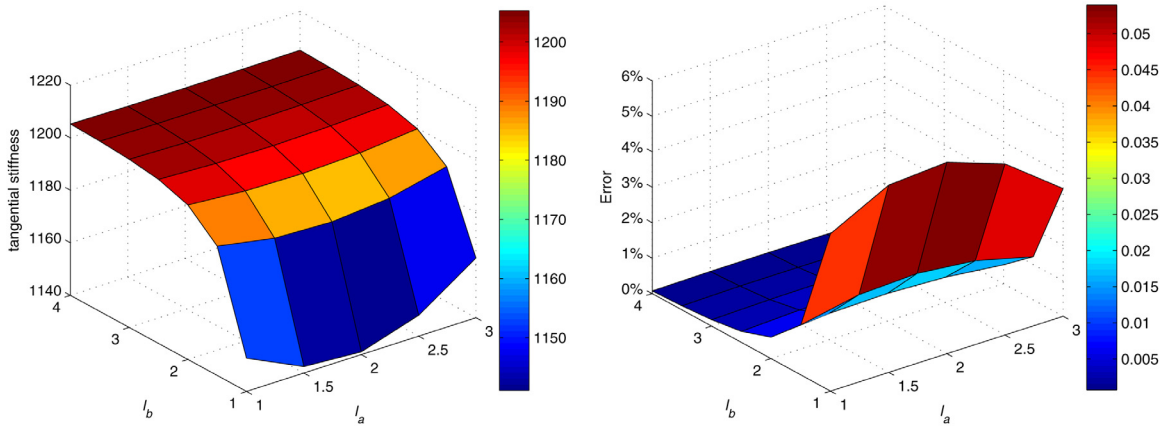

Fig. 10. The experimental set-up for stiffness test

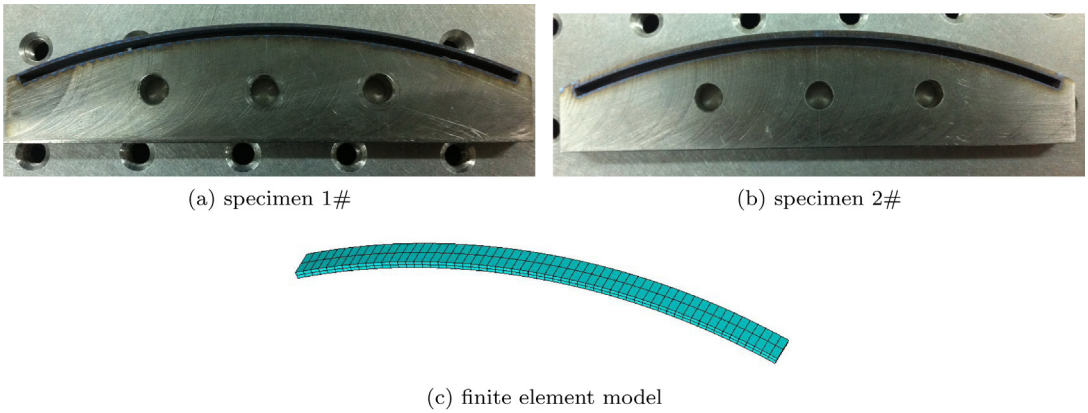

(a) specimen 1# (b) specimen 2#

(c) finite element model

Fig. 12. The test specimens and FE model of the flexible element

4.2. The stiffness verification

The experimental study and FE simulation are discussed here. First, the radial and tangential stiffness of the flexible element is verified. The process is described as: imposing a force which varies over a reasonable interval on the finite element model and the specimen of the flexible element and measuring the displacement of the loading point; thus comparing the theoretical displacement with the experimental and simulation results. Then, the stiffness of the integral flexible structure is verified in a similar way.

The experimental set-up used to test the stiffnesses of the flexible element and the integral flexible structure is shown in Fig. 11. This experimental set-up consists of a load-cell, a 1-D translation stage for mounting the load-cell, a high-precision optical grating displacement sensor and a PC computer loaded with LABVIEW software as the data collector. The data, including force and displacement data measured by the load-cell and displacement sensor respectively, are collected by the computer through a serial port(RS232). The homebuilt program based on LABVIEW is developed to collect the force and displacement data simultaneously and automatically, which could minimize the reading errors.

The specimens and finite element model of the flexible element and the integral flexible structure are shown in Fig. 12 and Fig. 13 respectively. The Titanium alloy material(TC4) with excellent mechanical and fatigue properties is adopted here to manufacture these specimens. The mechanical properties of TC4 are: the elastic modulus $E = 105GPa$, the Poisson ration $\nu = 0.31$ and the density $\rho = 4430kg \cdot m^{-3}$. The geometric properties of these specimens are listed in Table 1.

4.2.1. The element stiffness verification

First, the radial stiffness of the flexible element is verified through FE simulation and experiments. For the flexible element(specimens 1# and 2#), a radial force F_r is imposed on the central point of the specimen and its finite element model, where the variation interval of the radial force is (5*N*, 20*N*) for the specimen 1# and (10*N*, 60*N*) for the specimen 2#. The linear and nonlinear analysis using ANSYS software are performed. Then, the tangential stiffness of the flexible element is verified only through FE simulation. A tangential force F_t varying in (50N,150N) and (100N,200N) is imposed on the finite element model of specimens 1# and 2# respectively and the linear and nonlinear FE simulation are carried out. The test and FE simulation results for the specimens 1# and 2# are shown in Fig. 14 and Fig. 15. The radial and tangential stiffness are listed in Table 2, where the tested and nonlinear stiffness are obtained using the linear least square fit method. Here, we should note that in order to simplify the experimental equipment, only the radial stiffness is verified in this experiment.

Table 1
The geometric properties

	Element		Integral	
	1#	2#	3#	4#
arch number	–	–	5	6
Width (mm)	8	8	5	5
Thick (mm)	0.75	1.5	0.5	0.5
Radius(mm)	146.25	146.25	48.75	48.75
$\theta(^\circ)$	22.5	22.5	–	–

Table 2
The stiffness for the flexible element

specimen	theoretical	tested	linear FEA	nonlinear FEA
1#-radial	55.89	47.00	55.99	45.55
2#-radial	381.75	343.24	380.03	347.54
1#-tangential	1355.7	–	1323.5	1206.2
2#-tangential	9149.7	–	8872.2	8849.6

Analyzing the results from Fig. 14 and Tab. 2, we can see that for the radial stiffness the theoretical results agree with the linear FEA results very well and the test results agree well with the nonlinear FEA results, which indicates that the theoretical model presented in this work is capable to predict the linear deformation but can not capture the geometrical nonlinear behavior of the flexible element. The stiffness error for specimen 1# is less than the specimen 2#. Fig. 15 show that the tangential stiffness is far greater than the radial stiffness and it does not exhibit obvious geometrical nonlinear behavior under those load conditions. In addition, the maximum tangential stiffness error between the theoretical and linear or nonlinear simulation results is less than 4%.

4.2.2. The integral stiffness verification

For the integral flexible structure(specimens 3# and 4#), the geometrical parameters are listed in Table 1. Since the geometrical features are different for different directions, the load should be imposed on different directions in order to obtain the corresponding stiffness. Considering the symmetrical characteristics of this flexible structure, the test directions are shown in Fig. 16, where the specimen 3# has five test directions and the specimen 4# has three test directions. With a concentrated force *F* imposed on the edge of this flexible structure(see Fig. 11(b)), the variation interval of the force is (10*N*, 160*N*) for the specimen 3# and (50*N*, 250*N*) for the specimen 4#. In addition, the linear and nonlinear FE simulation are performed, where the FE model and boundary condition are identical with the experiments. The test and FE simulation results

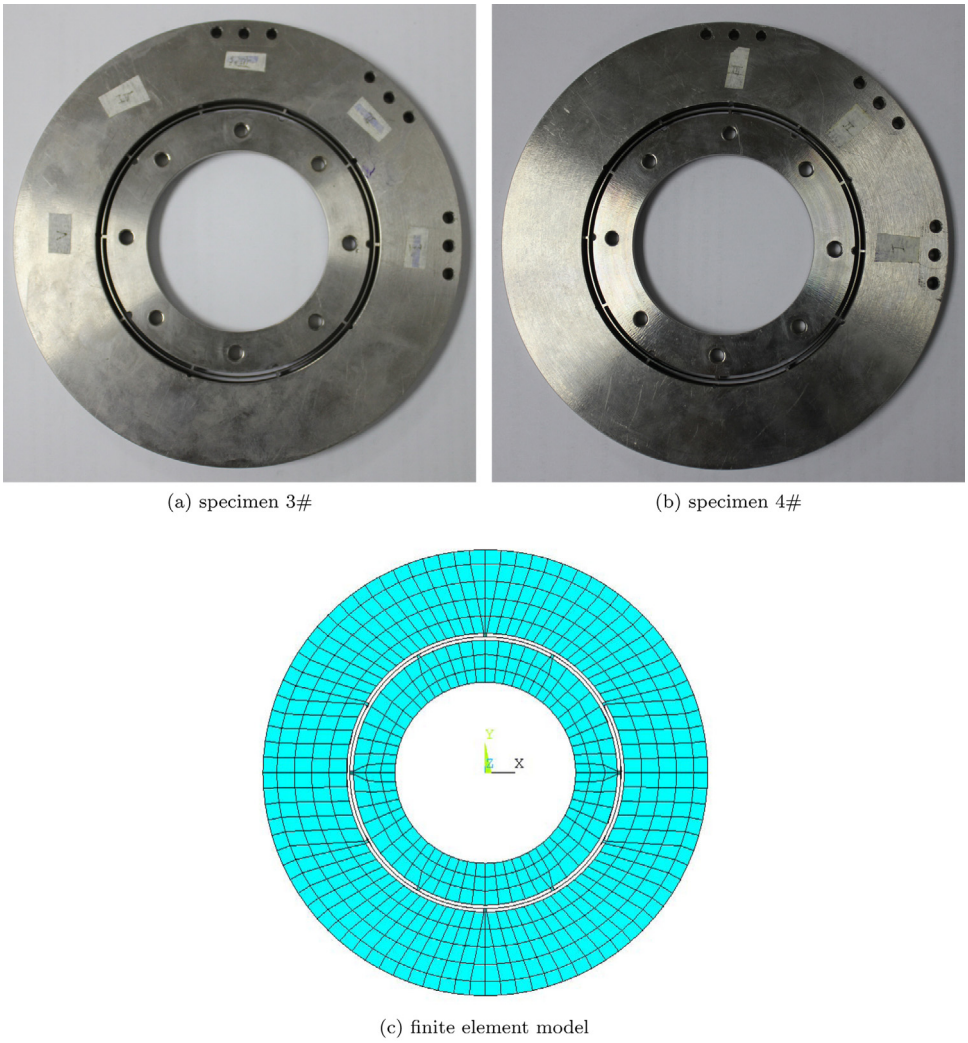

(a) specimen 3# (b) specimen 4#

(c) finite element model

Fig. 13. The test specimens and FE model of the integral flexible structure

for the specimens 3 # and 4 # are shown in Fig. 17 and their stiffness are listed in Table 3.

Fig. 17 show that the integral stiffness for the two specimens in various test directions are basically identical and the errors within these directions are less than 2%, which agrees with the stiffness model (26). The errors between the theoretical and linear or nonlinear simulation results are less than 4% for specimen 3 # and less than 3% for specimen 4 #. Since the stiffness are big enough when

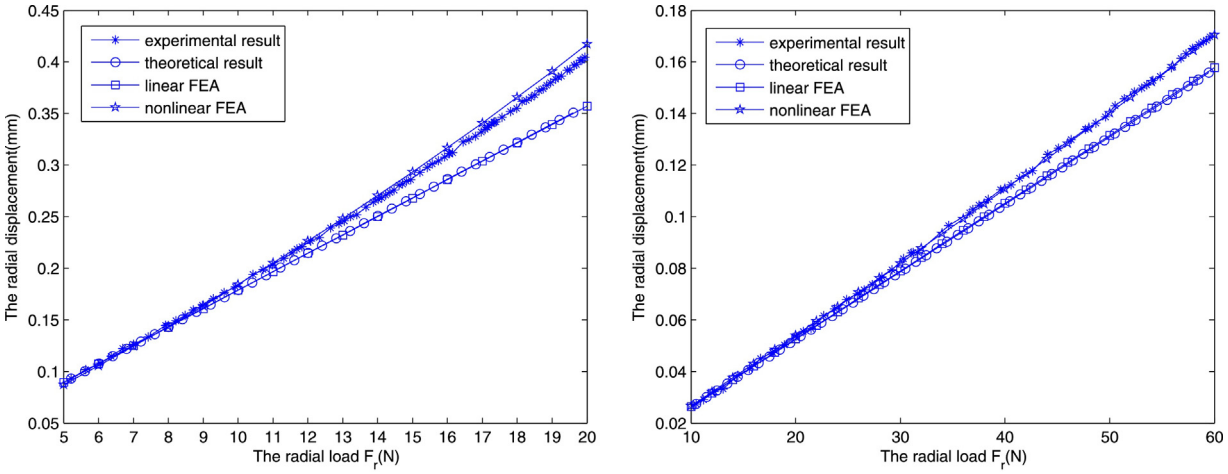

(a) specimen 1# (b) specimen 2#

Fig. 14. The test and simulation results for the radial stiffness of flexible element

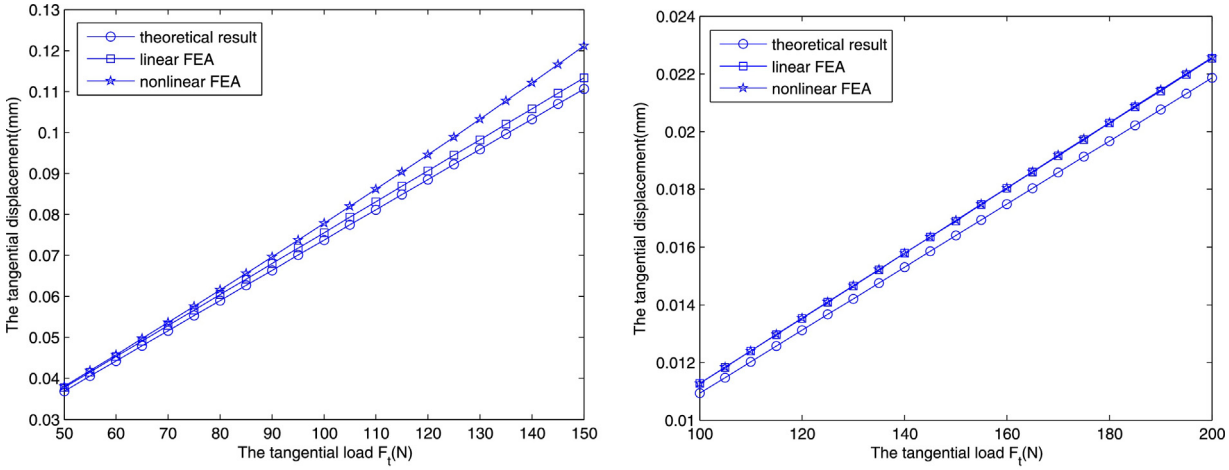

Fig. 15. The simulation results for the tangential stiffness of flexible element

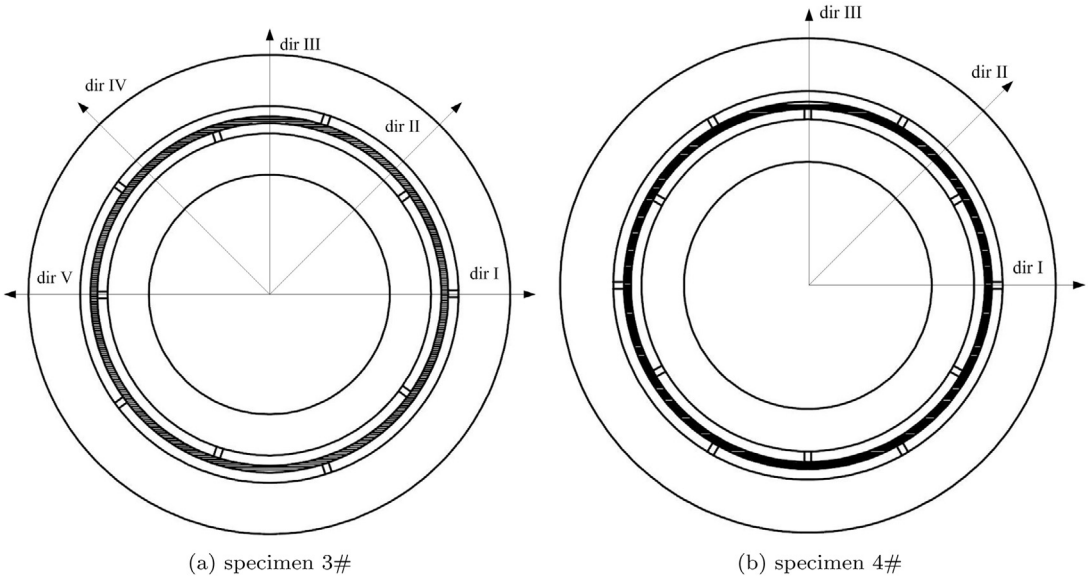

Fig. 16. The test directions for the circular-arch flexible structure

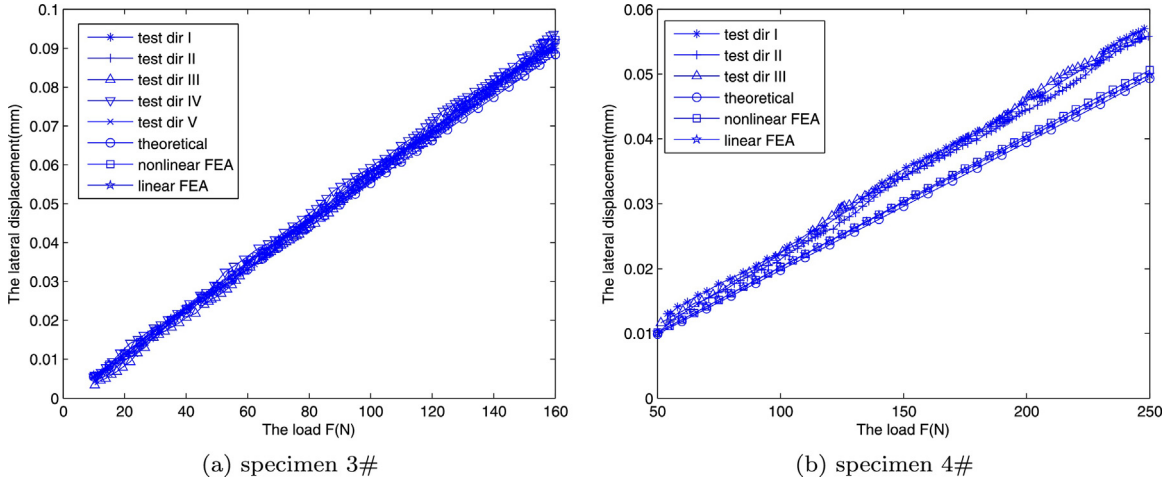

Fig. 17. The test and simulation results for the integral flexible structure

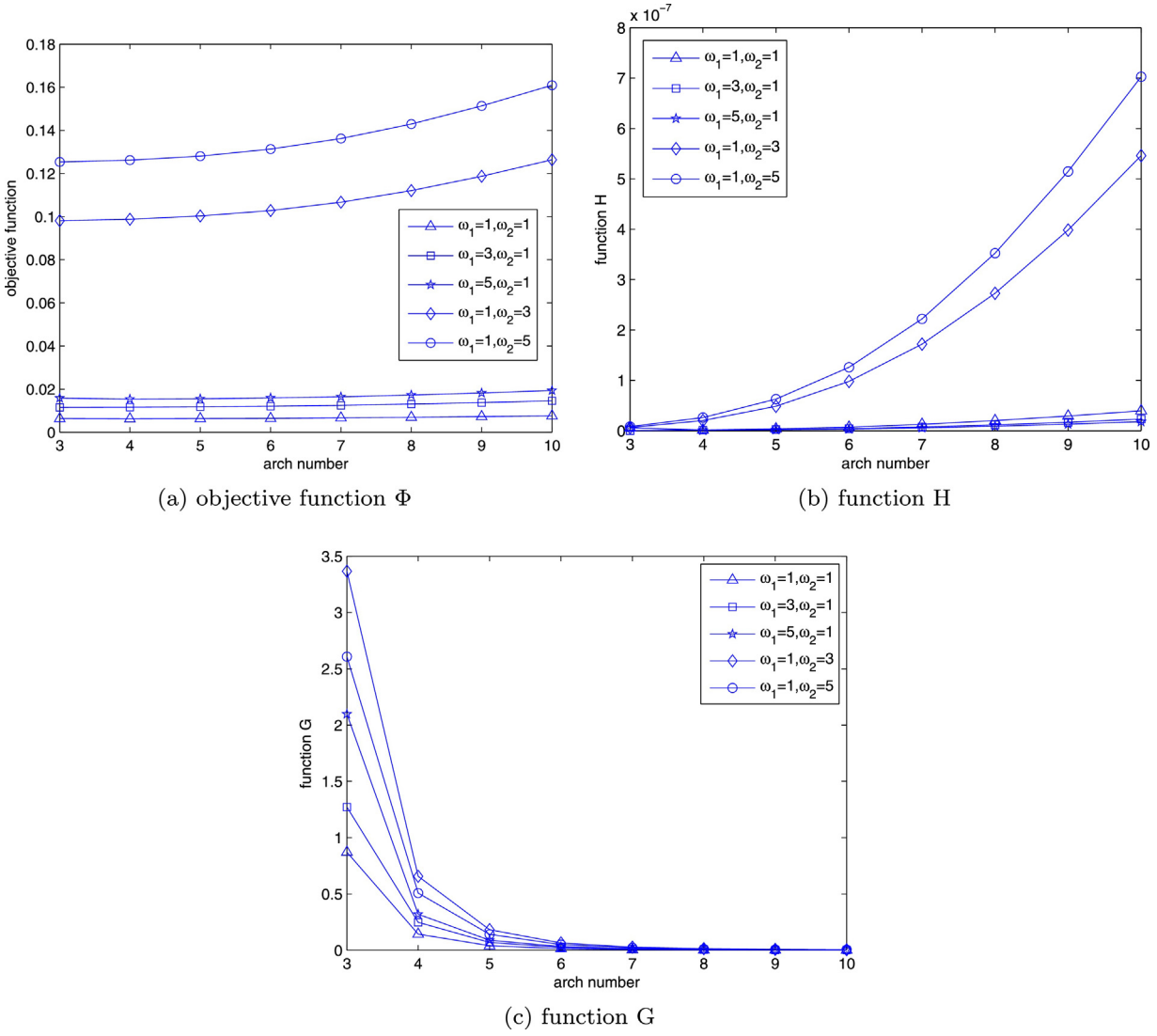

Fig. 18. The objective function Φ and function H and G vs. arch number

Table 3
The stiffness for the integral flexible structure

specimen	theoretical	tested	linear FEA	nonlinear FEA
3 # – *I*	1810.2	1749.8	1768.3	1736.4
3 # – *II*	1810.2	1734.6	1767.3	1736.3
3 # – *III*	1810.2	1718.2	1742.9	1736.3
3 # – *IV*	1810.2	1711.5	1741.6	1736.0
3 # – *V*	1810.2	1711.5	1740.5	1735.2
4 # – *I*	5069.2	4381.8	5023.5	4939.7
4 # – *II*	5069.2	4389.9	5090.3	5001.5
4 # – *III*	5069.2	4319.8	5058.0	4969.9

Table 4
The parameters of candidate materials

material no	E (GPa)	ν	ρ (kg/m^3)	α $(10^{-6}/K)$
1(6061)	69	0.33	2700	24
2(LC4)	75	0.35	2850	24.3
3(Ti-6Al-4V)	105	0.31	4430	9
4(Ti-5Al-2.5Sn)	110	0.31	4480	9
5(Ti-8Al-1Mo)	120	0.32	4370	8.5
6(45)	210	0.29	7820	12
7(Invar)	145	0.25	8100	1.6
8(Zerodur)	73	0.21	2210	0.03

the flexible structure acts as an integral part, the specimens 3 # &4 # do not exhibit obvious geometrical nonlinear behavior under those load conditions, which indicates that the presented stiffness model can be used to predict the integral stiffness. However, the error between test results and theoretical or FE simulation results are evident, especially for specimen 4 #, which may be caused by the manufacture error.

4.3. *The verification of the continuous optimization algorithm*

In this section, we present the simulation results for the continuous optimization method described above. The circular-arch flexible structure is used as the lateral support of the mirror. The model (35) is used to optimize the material and geometrical parameters of the flexible structure, where the parameters of the candidate materials are listed in Table 4 and the range of the geometrical parameters are: $R = 60$, $1 \le b \le 15$, $0.3 \le t \le 0.8$, units:(mm), and the external force $F = 200N$, the gravity of the mirror. The mirror's material parameters are listed in the last line of Table 4. We explore the influence of the weighted factors ω_1 and ω_2 on the objective function Φ and on function G and H, and compare the optimal results from the model(35).

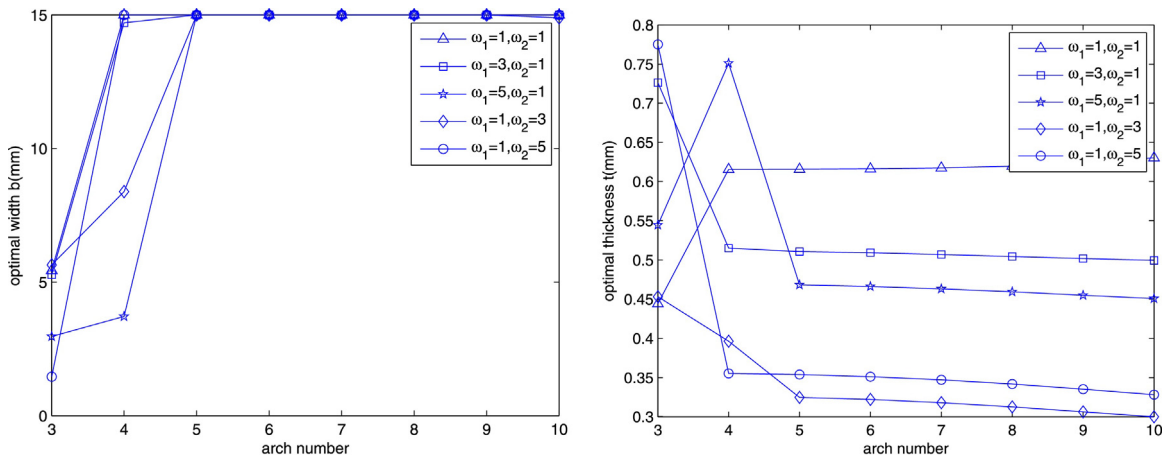

(a) optimal width (b) optimal thickness

Fig. 19. The optimal width and thickness

Table 5
The optimal material number

arch no	$\omega_1=1$ $\omega_2=1$	3 1	5 1	1 3	1 5
3	6	7	6	6	6
4	7	7	7	6	6
5	7	7	7	6	6
6	7	7	7	6	6
7	7	7	7	6	6
8	7	7	7	6	6
9	7	7	7	6	6
10	7	7	7	6	6

The objective function Φ as well as function H and G for different ω_1 and ω_2 combinations are shown in Fig. 18. As the arch number n increases, the objective function Φ and function H increase whereas the function G decreases for all the $\omega_{1,2}$ combinations. This indicates that the thermal stress imparting on the mirror increases while the rigid body displacement decreases. In addition, the variation of ω_1 or ω_2 have a greater impact on function H than G as the arch number increases.

For each ω_1 and ω_2 combination case, the optimal material number is listed in Table 5 and the optimal width and thickness are shown in Fig. 19. Fig. 19 shows that when $n \leq 6$, the optimal results vary greatly as ω_1 or ω_2 changes, while $n > 6$, the optimal results reach almost the same value for each case. Moreover, Table 5 shows the discrete optimal material for each case can be easily obtained from this continuous optimization model, indicating that the linear $\sum x_i = 1$ and nonlinear constraints $\sum x_i^2 = 1$ are adequate to force the continuous variables to the distinct values. However, since the stiffness expressions (14)(15) are nonlinear with respect to the geometrical parameters, the optimal width b and thickness t shown in Fig. 19 appear somewhat chaotic.

5. Conclusions

The circular-arch flexible structure has been investigated in this paper. The analytical model of the flexible element is derived using variational principle. The generalized formulation of the circular-arch flexible structure and a continuous optimization method are established. The artificial variables are introduced to relax the discrete material selection problem. The optimization of the circular-arch flexible structure is implemented by combining the material selection and geometry.

The experiment and numerical simulation are given to verify the mechanical model of the circular-arch flexible structure and the continuous optimization scheme presented in this paper. The experimental and FE simulation results show that theoretical stiffness of the flexible element and the integral flexible structure are capable of capturing their linear characteristics, and for the geometrical nonlinear deformation, there exist some errors. In addition, they also indicate that the stiffness of the circular-arch flexible structure are identical in the rotational directions except for some minor errors, which agree with the theoretical model. The optimization results demonstrate that the presented optimization scheme is able to realize the optimal design of this flexible structure considering the discrete material selection and geometry simultaneously. The linear and nonlinear constraints and the penal function of the optimization model are adequate to force the artificial variable to approach the distinct design.

Acknowledgments

The authors gratefully acknowledge the financial support of the NSFC(Grant No.11403023).

References

[1] Schwertz K, Burge J. Field Guide to Optomechanical Design and Analysis. Washington: SPIE Press; 2012.
[2] Paros JM, Weisbord L. How to design flexure hinge. Machine Design 1965;37(01):151–7.
[3] Cai K, Tian Y, Wang F, Zhang D, Shirinzadeh B. Development of a piezo-driven 3-DOF stage with T-shape flexible hinge mechanism. Robotics and Computer-Integrated Manufacturing 2016;37(2):125–38.
[4] Xu Q. Design, testing and precision control of a novel long-stroke flexure micropositioning system. Mechanism and Machine Theory 2013;70:209–24.
[5] Xu Q. A novel compliant micropositioning stage with dual ranges and resolutions. Sensors and Actuators A: Physical 2014;205:6–14.
[6] Zubir MNM, Shirinzadeh B, Tian Y. Development of a novel flexure-based microgripper for high precision micro-object manipulation. Sensors and Actuators A: Physical 2009;150(2):257–66.
[7] Hopkins JB, Vericella JJ, Harvey CD. Modeling and generating parallel flexure elements. Precision Engineering 2014;38(3):525–37.
[8] Yong YK, Lu T-F, Handley DC. Review of circular flexure hinge design equations and derivation of empirical formulations. Precision Engineering 2008;32(2):63–70.
[9] Smith ST, Badami VG, Dale JS, Xu Y. Elliptical flexure hinges. Review of Scientific Instruments 1997;68(3):1474–83.
[10] Wu Y, Zhou Z. Design calculations for flexure hinges. Review of Scientific Instruments 2002;73(8):3101–6.
[11] Lobontiu N, Paine JSN, Garcia E, Goldfarb M. Corner-Filleted Flexure Hinges. Journal of Mechanical Design 2000;123(3):346–52.
[12] Lobontiu N, Garcia E. Two-axis flexure hinges with axially-collocated and symmetric notches. Comput Struct 2003;81(13):1329–41.

[13] Lobontiu N, Garcia E. Analytical model of displacement amplification and stiffness optimization for a class of flexure-based compliant mechanisms. Comput Struct 2003;81(32):2797–810.
[14] Hopkins JB, Culpepper ML. Synthesis of precision serial flexure systems using freedom and constraint topologies (FACT). Precision Engineering 2011;35(4):638–49.
[15] DiBiasio CM, Hopkins JB. Sensitivity of freedom spaces during flexure stage design via FACT. Precision Engineering 2012;36(3):494–9.
[16] Hao G. Determinate Design and Analytical Analysis of a Class of Symmetrical Flexure Guiding Mechanisms for Linear Actuators. Journal of Mechanical Design 2016;139(1), 012301–012301.
[17] Zhang S, Fasse ED. A Finite-Element-Based Method to Determine the Spatial Stiffness Properties of a Notch Hinge. Journal of Mechanical Design 1998;123(1):141–7.
[18] Xu W, King T. Flexure hinges for piezoactuator displacement amplifiers: flexibility, accuracy, and stress considerations. Precision Engineering 1996;19(1):4–10.
[19] Yolder PR. Mounting Optics in Optical Instruments. 2nd edn. Washington: SPIE Press; 2008.
[20] Fata R, Kradinov V, Fabricant D. Flexure mounts for high-performance astronomical lenses. SPIE 2006;6269, 62695T-62695T-12.
[21] Froud TR, Tosh IAJ, Edeson RL, Dalton GB. Cryogenic mounts for large fused silica lenses. SPIE 2006;6273, 62732I-62732I-9.
[22] Saggin B, Tarabini M, Scaccabarozzi D. Infrared optical element mounting techniques for wide temperature ranges. Applied Optics 2010;49(3):542–8.
[23] Lim CW, Wang CM, Kitipornchai S. Timoshenko curved beam bending solutions in terms of Euler-Bernoulli solutions. Archive of Applied Mechanics 1997;67(3):179–90.
[24] Ahuett-Garza H, Chaides O, Garcia PN, Urbina P. Studies about the use of semicircular beams as hinges in large deflection planar compliant mechanisms. Precision Engineering 2014;38(4):711–27.
[25] Hvejsel CF, Lund E. Material interpolation schemes for unified topology and multi-material optimization. Structural and Multidisciplinary Optimization 2011;43(6):811–25.
[26] Hvejsel CF, Lund E, Stolpe M. Optimization strategies for discrete multi-material stiffness optimization. Structural and Multidisciplinary Optimization 2011;44(2):149–63.
[27] Kennedy GJ, Martins J. A laminate parametrization technique for discrete ply-angle problems with manufacturing constraints. Structural and Multidisciplinary Optimization 2013;48(2):379–93.
[28] Kennedy GJ. Discrete thickness optimization via piecewise constraint penalization. Structural and Multidisciplinary Optimization 2015;51(6):1247–65.
[29] Stegmann J, Lund E. Discrete material optimization of general composite shell structures. International Journal for Numerical Methods in Engineering 2005;62(14):2009–27.
[30] Yoder PR. Opto-Mechanical Systems Design. 2rd edn. Washington: CRC Press; 2006.
[31] Bauer R, Kuhn R. A Lateral Restraining Device for Large Telescope Mirrors. Journal of Modern Optics 1994;41(3):581–7.
[32] Qatu MS. Theories and analyses of thin and moderately thick laminated composite curved beams. International Journal of Solids and Structures 1993;30(20):2743–56.
[33] Bendse M, Sigmund O. Material interpolation schemes in topology optimization. Archive of Applied Mechanics 1999;69(9):635–54.
[34] Stolpe M, Svanberg K. An alternative interpolation scheme for minimum compliance topology optimization. Structural and Multidisciplinary Optimization 2001;22(2):116–24.
[35] Gill PE, Murray W, Saunders MA. SNOPT: An SQP algorithm for large-scale constrained optimization. SIAM REVIEW 2005;47(1):99–131.